Enhanced Crack Segmentation (eCS): A Reference Algorithm for Segmenting Cracks in Multicrystalline Silicon Solar Cells

Daniel Stromer ⬤, Andreas Vetter ⬤, Hasan Can Oezkan, Christian Probst, and Andreas Maier ⬤

Abstract—The annually produced quantity of solar modules has steadily increased over the past decades. Rising production speeds and the associated high throughput of wafers, cells, and modules will make an automatized quality inspection mandatory. In the case of visual optical inspection, automatized quality control by using machine vision is already possible. To localize cracks in solar cells, luminescence imaging is used, where several approaches for an automatized inspection exist, but a standard solution for an automatized inspection algorithm is not yet available. This is, in particular, true for multicrystalline solar cells, where the grainy structures in the luminescence images are hard to distinguish from small cracks. Another obstacle in automatic crack analysis is that reference segmentation algorithms are generally not publicly available. Accordingly, a new algorithm can hardly be compared by ranking it to an existing standard. In this paper, we adapted the vesselness algorithm for automatic processing of electroluminescence images of multicrystalline silicon solar cells. Segmentation of cracks in multicrystalline solar cells with the proposed enhanced crack segmentation algorithm shows very promising results on the used database compared with three different commonly used approaches. Furthermore, the segmentation code is made publicly available, and we propose that this algorithm may serve as a reference algorithm, sparking further progress in automatized crack segmentation for multicrystalline silicon solar cells.

Index Terms—Crack detection, crack segmentation, electroluminescence (EL) imaging, multicrystalline solar cell imaging, photovoltaic (PV).

I. INTRODUCTION

ENERGY production based on sustainable resources is becoming increasingly important. As an example, consider the increase of renewable electricity production from 83.7 TWh in 2000 to 1178.2 TWh in 2015 [1], which even excludes hydro power. Photovoltaics (PV) may contribute a major part to future renewable energy supply. Despite a certain current political headwind, the relevance of "renewables" and PV will most likely continue to rise in the next decades. Some countries may even reduce their efforts in pushing renewables forward, as there are other countries in the world capable of closing this gap. As an example, the largest PV park in the world used to be in the USA (with 550 MW). Nowadays, several "Mega" PV parks with at least 1 GW (existing and planned) are located in three different countries: China, India, and the United Arab Emirates [2].

Following this trend, more and more solar modules will be sold, and production will further ramp up. Module costs have fallen by almost a factor of 5 between 2011 and 2018 (from 1.6 to 0.34 USD/Wp), and costs will be further optimized [3]. Thus, the importance of PV as an energy source will be further strengthened. One essential key for price reduction of solar modules is quality inspection, both at the laboratory scale (quality analysis, mainly to increase the efficiency of solar cells and modules) and inline in the factory (quality control, mainly to increase the yield of production). Solar modules have to be a mass product in order to contribute considerably to a "renewable energy future," and hundreds or thousands of solar modules (each with a size of about 2 m^2) have to be assembled in PV parks. This number of modules is necessary in order to collect enough sunlight for producing electricity in a significant amount (e.g., replacing a conventional power plant). Accordingly, imaging methods, allowing a fast assessment of solar cells, modules, or even PV parks, are of special interests for a further commercial success story of PV.

Commonly used imaging methods for quality inspection of solar cells and modules [4] are based on infrared measurements [5]–[8], luminescence imaging [9]–[12], and optical inspection such as in the visible or near-infrared range, or even a combination of different imaging methods [13]–[20]. For quality control, all imaging methods need to be fast, as cell production has generally a throughput of at least one cell per second. Manufacturers aim for higher throughputs to further reduce the production costs per cell, and those are too high for a manual quality control. Instead, a fully automatized evaluation of the images is desirable. Different subtasks during the evaluation are necessary, such as the automatized detection of the cell edges and registration [21], [22], automated detection of rear contact voids [23], or automated assessment of the overall cell or module quality [24], [25].

One important possible fault during production is cracks [26]–[28], for example, induced by mechanical force when handling the solar cells or modules. A fast way of detecting such cracks

on the cell or module is given by electroluminescence (EL) imaging. Accordingly, several algorithms have been proposed for an automatized segmentation of cracks in EL images. Jean *et al.* [29] proposed an approach on several tools, including a thresholding tool and a binary large object tool. A major disadvantage of their approach is that a differentiation between cracks and other defects in the EL images is difficult. Similar results are true for the study of Lin *et al.* [30]. More promising results were reported by Tsai *et al.* [31] by using a self-referencing scheme based on Fourier image reconstruction. However, the study did not state the minimum crack size that can be identified with this approach. Sparatu *et al.* [32] applied two-dimensional (2-D) matched filters, which were taken from intensity profiles of cracks in EL images. They reported a crack detection rate of 90%, with an elongation of the cracks of at least 3 cm. Unfortunately, the study did not mention the runtime of the algorithm or a measurement of overrejection. Using an anisotropic diffusion filter, Anwar and Abdullah [33] were able to enhance cracks in EL images. The cracks could be segmented more easily, and good detection rates were obtained by a successive shape classification. The runtime was unfortunately rather high with 4.1 s for a 1178×1178 pixel image.

In summary, the correct classification of small cracks is a serious issue, especially for multicrystalline cells, where normal crystallographic defects may be incorrectly classified as crack by segmentation algorithms. To this point, there is no reference algorithm publicly available, and existing software programs such as dataArtist [34] do not yet provide definite results. In addition, a comparison of developed algorithms with industrial systems or products is hardly possible, as the underlying algorithms and resulting metrics are kept secret.

The aim of this work is to overcome this issue and to propose a reference segmentation algorithm for crack detection in EL images of solar cells. To do so, we tested an algorithm proposed by Frangi *et al.*, which is very commonly used in medical imaging to detect blood vessels. We adapted the algorithm to fit it to the needs of crack segmentation in EL images of solar cells. We thoroughly describe the algorithm and publish the code online. We hope that this will help the scientific community to better assess different segmentation algorithms and, accordingly, will help to improve automated detection of cracks in EL images of solar cells.

II. MATERIALS AND METHODS

A. Samples and Preprocessing

The samples were standard multicrystalline solar modules measured at the same electric current. Fig. 1 shows an unprocessed EL image, where the orange arrow points to a crack. An image contains a region slightly bigger than one single cell. In total, 47 images with a resolution of 1024×1024 pixel were selected for a detailed analysis. Here, seven images show no defects, and 40 images show cracks with different elongations and orientations. All images show commercially produced cells, and hence, the database does not include artificial induced cracks. Crack sizes range from about 20 mm to cracks covering the entire length of the cell. Smaller cracks (< 20 mm) are often rather difficult to clearly differentiate from noncrack structures
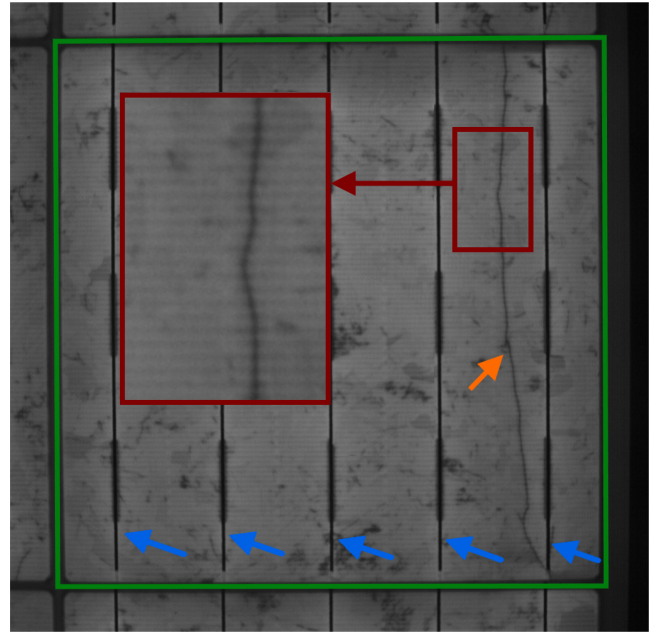

Fig. 1. EL image of a multicrystalline silicon solar cell with crack. The crack is denoted in orange. The blue arrows point to the busbars, while the greenish box marks the border of the cell to be inspected. The red box shows a zoom of the crack area highlighting the sinusoidal gridline intensities changing from gray to black in the vertical direction.

and were accordingly not part of this study. The cracks were manually labeled by an expert for further evaluations, and the labels were stored as binary masks.

To evaluate the algorithm for lower input resolutions, the experiments were also performed on downsized versions of the originals. In addition to measurements with the original image size, the influence on the algorithm's accuracy when downscaling (bilinear interpolation) by a factor of 0.75 (768×768 pixel) and 0.5 (512×512 pixel) was tested.

The appearance of such EL images can negatively affect the accuracy of the final crack detection algorithm. To enhance the quality of the results, the images were preprocessed by applying three subsequent steps, which are described in the following.

Fourier filtering was used to reduce the influence of gridlines in the EL images. Gridlines appear as a sinusoidal wave along the vertical axis of the image (the red box in Fig. 1), and setting certain frequencies in the Fourier domain to zero diminishes the small intensity changes. Without smoothing the gridlines, a subsequent crack segmentation can have an increased number of false positives (FPs) because even small intensity changes can lead to a response in non-crack regions of the image.

Next, the borders of the cell (the green box in Fig. 1) and the busbars (blue arrows in Fig. 1) were detected by binarizing the image and applying morphological filters [35] with vertical and horizontal line structuring elements of a certain thickness. Here, the structuring elements' kernels were determined empirically. Selecting this region of interest is necessary because cracks outside the cell must not be considered. Furthermore, the busbars have a crack-like structure in the image, and algorithms might mark them as cracks.

As all images of the underlying database use only about half of the 8-bit grayscale range, histogram equalization was applied

to stretch out the intensity range [36]. This step can be ignored if the images use the entire grayscale. Finally, a bilateral filter [37] was used to decrease noise and smooth rather homogeneous areas, while simultaneously preserving edges.

A common aspect of all methods is that they are computationally inexpensive, which is an important requirement for real-time processing on a conveyor belt.

B. Crack Segmentation

Nowadays, machine-learning algorithms achieve high accuracies in image-based defect detection. However, these algorithms are "data-hungry," which means that the training database must contain a large number of corrupted as well as uncorrupted images. Because this is usually never the case at the start of production, and manual labeling is also very time-consuming, an unsupervised crack segmentation algorithm can be applied to highlight cracks and crack-like structures. The images segmented by these unsupervised algorithms help drastically lower the amount of manual labeling work and, thus, allow to set up a database more quickly.

In comparison with monocrystalline silicon solar cells, crack segmentation is especially challenging for multicrystalline cells. The grainy structure can lead to a high false positive rate (FPR), especially when using methods that do not take the crack's shape into account. An example for such an algorithm is Otsu's thresholding [38], as well as other techniques, where a global threshold value is used for segmentation. Therefore, taking the image intensities as well as the shape of the object into account can be advantageous.

1) Vesselness Filtering: A method, which is commonly used in medical imaging for vessel segmentation, is vesselness filtering [39]. The main goal of this technique is to highlight vessels, which appear like tubular structures in images. Since the human vasculature has different thicknesses, it is essential to introduce multiscale measurement with certain scales. Cracks show the same tubular appearance in EL images; however, their thickness varies much less compared with vessels. The vesselness algorithm utilizes the eigenvalues of an input image's Hessian matrix $\mathbf{H}$ to calculate a probability map for vessels and background. As higher order derivatives are highly sensitive to noise, the components of $\mathbf{H}$ are Gaussian blurred with a certain scale σ. The Gaussian second-order derivative in the x-direction at pixel $\mathbf{p}$ can be computed by

$$\frac{\delta^2}{\delta x^2} I_G(\mathbf{p}, \sigma) = \frac{\delta}{\delta x^2} G(\sigma) * I(\mathbf{p}) \tag{1}$$

where I is the input image, and $G(\sigma)$ is an isotropic 2-D Gaussian distribution function, which is written as

$$G(\mathbf{p}, \sigma) = \frac{1}{2\pi\sigma^2} \exp\left(-\frac{x^2 + y^2}{2\sigma^2}\right). \tag{2}$$

The Hessian matrix of I is then calculated by

$$\mathbf{H}(\mathbf{p}, \sigma) = \begin{bmatrix} \frac{\delta^2}{\delta x^2} I_G(\mathbf{p}, \sigma) & \frac{\delta^2}{\delta x \delta y} I_G(\mathbf{p}, \sigma) \\ \frac{\delta^2}{\delta y \delta x} I_G(\mathbf{p}, \sigma) & \frac{\delta^2}{\delta y^2} I_G(\mathbf{p}, \sigma) \end{bmatrix}. \tag{3}$$

Next, the eigenvalues λ_1, λ_2 ($|\lambda_1| < |\lambda_2|$) of $\mathbf{H}$ are calculated by applying singular value decomposition. Considering an image where cracks appear as dark tubular structures on a bright background, both eigenvalues should be greater than zero in the case of a crack. When a pixel lies in a crack region, λ_1 is a small value (ideally zero), whereas λ_2 is large. From the eigenvalues, the "blobness measure" $R_B = |\lambda_1| \cdot |\lambda_2|^{-1}$ is calculated to differentiate vessels from blob-like structures. The "second-order structureness" $S = \sqrt{\lambda_1^2 + \lambda_2^2}$ yields information about the contrast between cracks and their environment, where the result is close to zero if no structure exists in the background. On the other hand, this measure will be larger in the case of a crack because λ_2 will have a high magnitude.

Next, a crack probability for each pixel $\mathbf{p}$ and σ is calculated by

$$V(\mathbf{p}, \sigma) = \begin{cases} 0, & \text{if } \lambda_1 \approx 0 \\ \exp\left(-\frac{R_B^2}{2\beta^2}\right)\left(1 - \exp\left(-\frac{S^2}{2c^2}\right)\right), & \text{if } \lambda_1 > 0 \end{cases} \tag{4}$$

where β and c denote constant parameters controlling the algorithms sensitivity. The resulting probability map shows values close to "1" where a crack is located and small values in background areas with low response.

Finally, $V(\mathbf{p}, \sigma)$ is calculated for multiple scales $\sigma_{\min}, ..., \sigma_{\max}$, and the maximum probability over all scales is considered as the final output according to

$$V_{\text{res}}(\mathbf{p}) = \max_{\sigma_{\min} < \sigma < \sigma_{\max}} V(\sigma). \tag{5}$$

To binarize the resulting probability map, global thresholding with a value t is applied splitting the image into crack and background.

2) Enhanced Crack Segmentation (eCS): We proposed an adaption of the vesselness filter algorithm used to segment pages of a scanned historical book within X-ray volumes [40], which can also be utilized for crack segmentation. The original vesselness algorithm was developed to segment vessels having randomly curved structures with changing diameters. However, when investigating cracks, their shape can be described by an elongated thin rather long tubular structure. To take this into account, the isotropic scale of the Gaussian distribution $G(x, y; \sigma)$ can be adapted to better fit the cracks' appearance by introducing an anisotropic scale. The anisotropic 2-D Gaussian distribution is calculated by

$$G_a(\mathbf{p}; \sigma_x, \sigma_y) =$$
$$\frac{1}{2\pi\sigma_x\sigma_y\sqrt{1-\rho^2}} \exp\left(-\frac{1}{2(1-\rho^2)}\left[\frac{x^2}{\sigma_x^2} + \frac{y^2}{\sigma_y^2} - \frac{2\rho xy}{\sigma_x\sigma_y}\right]\right) \tag{6}$$

with ρ denoting the correlation of σ_x and σ_y. For simplification, we consider only distributions that are aligned with the x- and y-axes such that σ_x and σ_y become uncorrelated with $\rho = 0$. As a result, (6) reduces to

$$G_a(\mathbf{p}; \sigma_x, \sigma_y) = \frac{1}{2\pi\sigma_x\sigma_y} \exp\left(-\frac{x^2}{2\sigma_x^2} - \frac{y^2}{2\sigma_y^2}\right). \tag{7}$$

Next, we define a degree of asymmetry n specifying the factor of anisotropy between σ_x and σ_y of the Gaussian filter, where $\sigma_x = n \cdot \sigma_y$ ($n \geq 1$) focuses on cracks elongated in the horizontal

This article has been accepted for inclusion in a future issue of this journal. Content is final as presented, with the exception of pagination.

4

IEEE JOURNAL OF PHOTOVOLTAICS

direction, and $\sigma_y = n \cdot \sigma_x$ $(n \geq 1)$ highlights vertical cracks. Inserting this into (7) yields

$$G_{ax}(\mathbf{p}; n, \sigma_x) = \frac{1}{2\pi n \sigma_x^2} \exp\left(-\frac{n^2 x^2 + y^2}{2n^2 \sigma_x^2}\right) \qquad (8)$$

for horizontal cracks, whereas the vertical crack enhanced version is calculated by

$$G_{ay}(\mathbf{p}; n, \sigma_y) = \frac{1}{2\pi n \sigma_y^2} \exp\left(-\frac{x^2 + n^2 y^2}{2n^2 \sigma_y^2}\right). \qquad (9)$$

If $n = 1$, the asymmetry vanishes, and the adapted vesselness result will become identical to the original vesselness filter. As the crack thicknesses are the same for both directions, we set $\sigma_x = \sigma_y = \sigma_a$.

In total, the proposed algorithm is controlled by five parameters: β, c, σ_a, n, and t. In summary, the adapted algorithm with the introduced degree of asymmetry (eCS) should enhance the segmentation of crack parts, which are horizontally and vertically elongated.

III. RESULTS

For evaluating the proposed eCS algorithm, a comparison with two other approaches was performed: global thresholding and original vesselness filtering with $\sigma = (1, 2)$ (Frangi12). For the eCS algorithm, the variable parameters were optimized by a grid search aiming for a small number of FPs and a high number of true positives (TPs) leading to $\beta = 0.5$, $c = 0.05$, $n = 1.5$, $\sigma_a = 2.0$, and $t = 0.9$ for all eCS algorithms. For this, a test set of 40 images and a validation set of seven images were used (randomly assigned, both sets containing crack and noncrack images), and the FP and TN were averaged over all results. In addition, the algorithm was tested with $n = 2.0$ (eCS2) and $n = 2.5$ (eCS2.5). As the anisotropic character of the eCS algorithms can lead to decreased segmentation results for diagonal crack structures, we also tested the algorithms for a $45°$ rotated version of the image. Due to that grid fingers are horizontally and bus bars vertically aligned, this adaption can also reduce FPs through those structures.

To evaluate the algorithms, we use the receiver operating characteristic (ROC) curve, which shows the true positive rate (TPR) and the FPR for different discrimination thresholds. Furthermore, the area under curve (AUC), which is an accuracy measurement for segmentation algorithms, was calculated. Higher AUC values indicate better results, where an AUC of 1 is an optimal result and 0.5 is comparable with a random guess. To retrieve more insights on the performance of the algorithms' results, the precision, recall, and accuracy (ACC) are calculated by averaging over the entire database.

We will now highlight the main results. According to Fig. 2, global thresholding shows the lowest AUC of 0.2266. This approach ensures that most of the crack pixels are segmented as such, but the FPR is dramatically large. This is in agreement with previous results from other groups [29], [30]. A discrepancy between a large TPR and a low FPR is seen for most algorithms and is common to most segmentation problems. However, this degree of discrepancy is rather striking in the
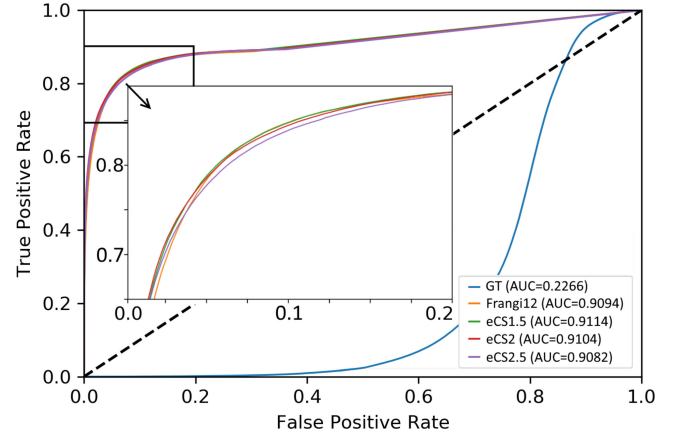

Fig. 2. ROC curves and the respective AUC results for the evaluated algorithms. Global thresholding performs badly compared with the vesselness approaches. eCS1.5 shows the best ROC curve and achieves the highest AUC score.

case of crack segmentation in EL images, mainly due to the multicrystalline structures. All four other algorithms show drastically better results than global thresholding. eCS1.5 achieved the best AUC (0.9114) compared with Frangi12 (0.9094) and all other eCS versions. The curves in Fig. 2 strengthen this observation, where it can be seen that eCS1.5 achieves the best TPR-to-FPR ratio. The runtime of global thresholding was the fastest (0.005 s) and eCS2.5 the slowest (0.668 s); however, all methods took less than a second on a standard laptop CPU (Intel(R) Core(TM) i7-6700K, 32-GB DDR4 RAM). As a remark, the runtime of the preprocessing steps was 0.6 s. Further runtime optimization can be done by processing the data in parallel on a GPU.

Next, the segmentation results of a randomly chosen crack image shown in Fig. 3(a) were visually inspected with a threshold t determined by the ROC analysis. Within the results, red regions denote pixels wrongly segmented as crack (FP), green regions denote correctly segmented cracks (TP), and orange areas missed crack pixels (false negatives; FN), whereas the numbers on top of the images correspond to the total pixel count for those regions. One can conclude that global thresholding (here, Otsu's method) [see Fig. 3(b)] is useless, as it is not capable of handling shaded areas and, thus, has a very high FP count. Standard vesselness filtering [see Fig. 3(c)] reduces the FP, while still segmenting the crack. eCS2 [see Fig. 3(e)] further reduces the FP and increases the TP, while eCS1.5 [see Fig. 3(d)] shows a very low FP count. eCS2.5 [see Fig. 3(e)] has the highest TP count, but also the FP increased. Neglecting Otsu's algorithm, eCS1.5 outperforms the other algorithms with respect to the pixel counts for FPs, while keeping the TP at the same level as Frangi12. Rotating the image by $45°$ shows the lowest FP and TP count and the highest FN count. Downsizing the image to half of the image size increases the number of TP, as well as the FP related to the total number of image pixels. The visual outputs furthermore correlate with the quantitative results from the ROC curve (see Fig. 2).

Table I shows the evaluation metrics for eCS1.5 compared with Frangi12. The results were averaged over the entire

This article has been accepted for inclusion in a future issue of this journal. Content is final as presented, with the exception of pagination.

STROMER *et al.*: eCS: A REFERENCE ALGORITHM FOR SEGMENTING CRACKS IN MULTICRYSTALLINE SILICON SOLAR CELLS
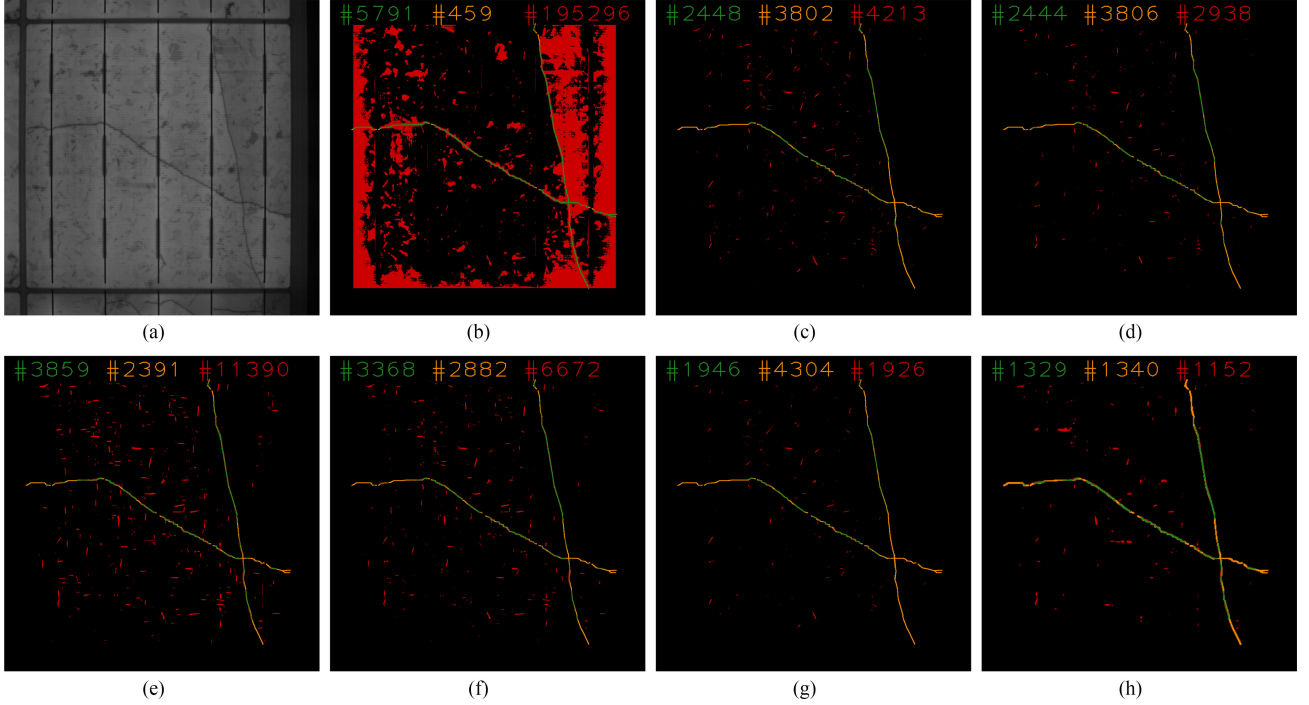
5

Fig. 3. Original EL image and the segmented results. Green indicates correctly segmented crack pixels (TP), orange indicates not segmented crack pixels (false negatives), and red indicates incorrectly segmented background (FP). Although Otsu has the highest TP score, it cannot handle shaded areas resulting in high FP. Frangi12 improves the FP, but shows decreased TP. eCS1.5 further decreases the FP, while keeping the TP at the same level. Increasing the degree of asymmetry results in higher TP and FP. Rotating the standard image by 45° results in decreased TP and FP, while downscaling the image by a factor of 2 increases the TP and FP related to the total number of image pixels. (a) Original EL image. (b) Otsu. (c) Frangi12 $- t = 0.7$. (d) eCS1.5 $- t = 0.9$. (e) eCS2.5 $- t = 0.9$. (f) eCS2 $- t = 0.9$. (g) eCS1.5_45° $- t = 0.9$. (h) eCS1.5_50% $- t = 0.9$.

TABLE I
EVALUATION METRICS OF THE PROPOSED eCS1.5 ALGORITHM
COMPARED WITH FRANGI12 FOR DIFFERENT SETTINGS

	Precision	Recall	ACC	AUC	Runtime [s]
eCS1.5_45°	**0.287**	0.345	**0.997**	0.9103	1.11
Frangi12_45°	0.210	0.410	0.996	0.9089	1.10
eCS1.5	0.245	0.436	0.996	**0.9114**	1.10
Frangi12	0.181	0.436	0.995	0.9094	1.09
eCS1.5_75%	0.166	0.478	0.995	0.8847	0.58
Frangi12_75%	0.125	**0.489**	0.992	0.8826	0.57
eCS1.5_50%	0.187	0.434	0.992	0.8402	0.25
Frangi12_50%	0.137	0.468	0.989	0.8400	**0.25**

database. The first two rows show results for 45° rotated images. The next two rows show the metrics for the standard input images. The last four rows show results for downscaled (factors 0.75 and 0.5) nonrotated images. This reduces the runtime for a single image by about a factor of 2 and 4, respectively, compared with the standard image size. The best precision and accuracy (ACC) is achieved by a 45° image rotation. The best AUC is achieved by eCS1.5, whereas Frangi12 downsized by a factor of 0.75 shows the best recall measure. It can be seen that downsizing the image by 25% halves the runtime for a single image; however, the accuracy gets slightly worse.

IV. DISCUSSION

Not surprisingly, global thresholding was not successful as a crack segmentation algorithm for EL images of multicrystalline

cells. Many other dark areas besides cracks result in a large FPR. The standard vesselness algorithm shows a significant improvement with an AUC of 0.9094. The eCS algorithms further increased the AUC up to 0.9114, where eCS1.5 achieved the best results with a very low count of FPs. The dramatic increase compared with Otsu's can be explained by the included shape information of cracks. As a remark, the presented values in this paper depend on the selected input parameters of the algorithms and the EL images. We believe that the results are representative as we did an initial grid search to evaluate the influence of the input parameters, and the given mean values are derived from 47 typical images, including noncrack images as well.

As a further remark, we want to mention that the proposed eCS algorithm works best for rather vertical or horizontal cracks if the degree of asymmetry increases. In reality, most of the diagonal cracks also consist of more vertical or more horizontal parts, which will be detected better with our adapted algorithm. A rotation of the image by 45° showed a decreased number of TPs; however, the number of FPs was also decreased. The decrease in the number of FPs can be explained by the fact that grid fingers are horizontally aligned, and by rotating the image, artifacts introduced by those structures are decreased.

The runtimes for the vesselness algorithms are all below 700 ms (excluding preprocessing taking 0.6 s), which is acceptable for inline characterization of solar cells, but an improvement of the runtime by using GPU's is desired. Downsizing the image improved the runtime; however, the accuracy slightly dropped. When using the algorithm in a production

environment, one has to trade off runtime versus accuracy, as well as take a look at the influence on a following crack classification or quantification step.

Additional postprocessing steps of the segmented images (e.g., outlier removal or morphological filtering) should further improve segmentation results. However, a final classification step, which is able to handle small outliers, is most likely required in any case. Here, eCS would show again its strength, as it strongly reduces the number of FP objects (cf., Fig. 3), making a final classification more straightforward than the other algorithms. The ratio of correctly segmented crack pixels (indicated by green in Fig. 3) and falsely segmented cracks (indicated by red) may give a better impression: for local thresholding, this ratio is 0.03; for standard vesselness, it is 0.58; and for eCS1.5, it is 0.83.

The resulting segmentation can build the basis for crack detection or quantification steps. By applying the proposed algorithm, the initial image information gets significantly reduced to a small subset of pixels that have to be classified to be crack or no crack. This could be solved by using methods like counting pixel areas (e.g., crack if area ≥ 25 pixel) or classification by applying recent machine-learning techniques [41], where the results of this work can be used as feature maps.

It has to be mentioned that adjusting the focus correctly is important for the segmentation algorithm. If defocussed, images become more blurry resulting in lower contrast. For the case of EL cracks, this means less pronounced or deep "valleys" in the images, which makes crack segmentation more difficult. The effect of defocussing may be counterbalanced to a certain degree by a threshold parameter. However, appropriate adjustment is an essential part of successful segmentation of cracks. This is rather easy to realize for inline imaging (due to the fixed position of camera and samples) but much more challenging for outdoor EL images.

V. CONCLUSION

The vesselness algorithm, a well-known reference algorithm in medical image segmentation, has been used for the first time for crack segmentation in EL images of polycrystalline solar cells. This algorithm has the advantage of having only few parameters (which may partly be derived from the image data), which has facilitated the success and the spread of the algorithm. We minimally adapted the vesselness algorithm to better suit it to the requirements as a crack segmentation filter in EL images. As a sidemark, our adaption should also give good results in other types of images as well. This should be true as long as the inspected cracks show an "extended elongation," i.e., the parts of the cracks resemble more lines than curves.

Furthermore, no reference algorithm has yet been set for crack segmentation in EL images. This has hampered an easy comparison of crack segmentation algorithms and, accordingly, the improvement of unsupervised crack detection. In summary, we propose the eCS as a reference algorithm. To do so, we thoroughly described the algorithm in this paper and published the code at https://www5.cs.fau.de/en/our-team/stromer-daniel/ photovoltaics/ so that it is accessible to the scientific community.

REFERENCES

[1] United Nations, *2018 Energy Statistics Pocket Book*. New York, NY, USA: United Nations Publications, 2018.

[2] List of photovoltaic power stations, "List of photovoltaic power stations—Wikipedia, the free encyclopedia," Aug. 20, 2018. [Online]. Available: https://en.wikipedia.org/wiki/List_of_photovoltaic_power_stations

[3] IW Group, "International Technology Roadmap for Photovoltaic Results." SEMI, Berlin, Germany, 2017.

[4] B. Du, R. Yang, Y. He, F. Wang, and S. Huang, "Nondestructive inspection, testing and evaluation for Si-based, thin film and multi-junction solar cells: An overview," *Renew. Sustain. Energy Rev.*, vol. 78, pp. 1117–1151, 2017.

[5] O. Breitenstein, J. Rakotoniaina, M. H. Al Rifai, and M. Werner, "Shunt types in crystalline silicon solar cells," *Prog. Photovolt.: Res. Appl.*, vol. 12, no. 7, pp. 529–538, 2004.

[6] J. Isenberg and W. Warta, "Realistic evaluation of power losses in solar cells by using thermographic methods," *J. Appl. Phys.*, vol. 95, no. 9, pp. 5200–5209, 2004.

[7] A. Vetter *et al.*, "Visualizing the performance loss of solar cells by IR thermography—An evaluation study on cigs with artificially induced defects," *Prog. Photovolt.: Res. Appl.*, vol. 24, no. 7, pp. 1001–1008, 2016.

[8] T. M. Pletzer, J. I. van Mölken, S. Rißland, O. Breitenstein, and J. Knoch, "Influence of cracks on the local current–voltage parameters of silicon solar cells," *Prog. Photovolt.: Res. Appl.*, vol. 23, no. 4, pp. 428–436, 2015.

[9] T. Trupke, R. Bardos, M. Schubert, and W. Warta, "Photoluminescence imaging of silicon wafers," *Appl. Phys. Lett.*, vol. 89, no. 4, 2006, Art. no. 044107.

[10] P. Würfel *et al.*, "Diffusion lengths of silicon solar cells from luminescence images," *J. Appl. Phys.*, vol. 101, no. 12, 2007, Art. no. 123110.

[11] M. Glatthaar *et al.*, "Spatially resolved determination of dark saturation current and series resistance of silicon solar cells," *Phys. Status Solidi (RRL)—Rapid Res. Lett.*, vol. 4, nos. 1/2, pp. 13–15, 2010.

[12] I. Zafirovska, M. K. Juhl, J. W. Weber, J. Wong, and T. Trupke, "Detection of finger interruptions in silicon solar cells using line scan photoluminescence imaging," *IEEE J. Photovolt.*, vol. 7, no. 6, pp. 1496–1502, Nov. 2017.

[13] M. A. Ordaz and G. B. Lush, "Machine vision for solar cell characterization," in *Proc. SPIE*, 2000, vol. 3966, pp. 238–249.

[14] M. Trautmann, M. Hemsendorf, C. Berge, C. Probst, and E. Rueland, "Non-contact microcrack detection from as-cut wafer to finished solar," in *Proc. 38th IEEE Photovolt. Spec. Conf.*, 2012, pp. 485–488.

[15] D.-M. Tsai and M.-C. Lin, "Machine-vision-based identification for wafer tracking in solar cell manufacturing," *Robot. Comput.-Integr. Manuf.*, vol. 29, no. 5, pp. 312–321, 2013.

[16] S. Wieghold, A. E. Morishige, L. Meyer, T. Buonassisi, and E. M. Sachs, "Crack detection in crystalline silicon solar cells using dark-field imaging," *Energy Procedia*, vol. 124, pp. 526–531, 2017.

[17] M. Demant *et al.*, "Microcracks in silicon wafers i: Inline detection and implications of crack morphology on wafer strength," *IEEE J. Photovolt.*, vol. 6, no. 1, pp. 126–135, Jan. 2016.

[18] T. Strauch, M. Demant, P. Krenckel, S. Riepe, and S. Rein, "Analysis of grain structure evolution based on optical measurements of mc si wafers," *J. Cryst. Growth*, vol. 454, pp. 147–155, 2016.

[19] S. Johnston *et al.*, "Correlating multicrystalline silicon defect types using photoluminescence, defect-band emission, and lock-in thermography imaging techniques," *IEEE J. Photovolt.*, vol. 4, no. 1, pp. 348–354, Jan. 2014.

[20] S. P. Harvey *et al.*, "Investigating pid shunting in polycrystalline silicon modules via multiscale, multitechnique characterization," *Prog. Photovolt.: Res. Appl.*, vol. 26, no. 6, pp. 377–384, 2018.

[21] A. Vetter, J. Hepp, and C. J. Brabec, "Automatized segmentation of photovoltaic modules in ir-images with extreme noise," *Infrared Phys. Technol.*, vol. 76, pp. 439–443, 2016.

[22] M. Hösel, R. R. Søndergaard, M. Jørgensen, and F. C. Krebs, "Fast inline roll-to-roll printing for indium-tin-oxide-free polymer solar cells using automatic registration," *Energy Technol.*, vol. 1, no. 1, pp. 102–107, 2013.

[23] K. Öğütman, K. O. Davis, H. Ali, S. R. Martell, and W. V. Schoenfeld, "Automated detection of rear contact voids in PERC cells with photoluminescence imaging," *Sol. Energy Mater. Sol. Cells*, vol. 179, pp. 31–35, 2018.

[24] A. Vetter *et al.*, "Lock-in thermography as a tool for quality control of photovoltaic modules," *Energy Sci. Eng.*, vol. 1, no. 1, pp. 12–17, 2013.

[25] J. Hepp, F. Machui, H.-J. Egelhaaf, C. J. Brabec, and A. Vetter, "Automatized analysis of ir-images of photovoltaic modules and its use for quality control of solar cells," *Energy Sci. Eng.*, vol. 4, no. 6, pp. 363–371, 2016.

[26] M. Köntges *et al.*, "Review of failures of photovoltaic modules," Int. Energy Agency, Paris, France, Rep. IEA-PVPS T13-01:2014, 2016.

[27] M. Abdelhamid, R. Singh, and M. Omar, "Review of microcrack detection techniques for silicon solar cells," *IEEE J. Photovolt.*, vol. 4, no. 1, pp. 514–524, Jan. 2014.

[28] M. Israil, S. A. Anwar, and M. Z. Abdullah, "Automatic detection of micro-crack in solar wafers and cells: A review," *Trans. Inst. Meas. Control*, vol. 35, no. 5, pp. 606–618, 2013.

[29] J.-H. Jean, C.-H. Chen, and H.-L. Lin, "Application of an image processing software tool to crack inspection of crystalline silicon solar cells," in *Proc. Int. Conf. Mach. Learn. Cybern.*, 2011, vol. 4, pp. 1666–1671.

[30] W.-J. Lin, Y.-H. Lei, and C.-H. Huang, "Automatic detection of internal defects in solar cells," in *Proc. IEEE Instrum. Meas. Technol. Conf.*, 2011, pp. 1–4.

[31] D.-M. Tsai, S.-C. Wu, and W.-C. Li, "Defect detection of solar cells in electroluminescence images using fourier image reconstruction," *Sol. Energy Mater. Sol. Cells*, vol. 99, pp. 250–262, 2012.

[32] S. Spataru, P. Hacke, and D. Sera, "Automatic detection and evaluation of solar cell micro-cracks in electroluminescence images using matched filters," in *Proc. IEEE 43rd Photovolt. Specialists Conf.*, 2016, pp. 1602–1607.

[33] S. A. Anwar and M. Z. Abdullah, "Micro-crack detection of multicrystalline solar cells featuring an improved anisotropic diffusion filter and image segmentation technique," *EURASIP J. Image Video Process.*, vol. 2014, no. 1, 2014, Art. no. 15.

[34] K. G. Bedrich, M. Bliss, T. R. Betts, and R. Gottschalg, "Electroluminescence imaging of PV devices: Camera calibration and image correction," in *Proc. IEEE 44th Photovolt. Spec. Conf.*, 2017, pp. 1–6.

[35] R. M. Haralick, S. R. Sternberg, and X. Zhuang, "Image analysis using mathematical morphology," *IEEE Trans. Pattern Anal. Mach. Intell.*, vol. PAMI-9, no. 4, pp. 532–550, Jul. 1987.

[36] S. M. Pizer *et al.*, "Adaptive histogram equalization and its variations," *Comput. Vis., Graph., Image Process.*, vol. 39, no. 3, pp. 355–368, 1987.

[37] C. Tomasi and R. Manduchi, "Bilateral filtering for gray and color images," in *Proc. 6th Int. Conf. Comput. Vis.*, 1998, pp. 839–846.

[38] N. Otsu, "A threshold selection method from gray-level histograms," *IEEE Trans. Syst., Man, Cybern.*, vol. SMC-9, no. 1, pp. 62–66, Jan. 1979.

[39] A. F. Frangi, W. J. Niessen, K. L. Vincken, and M. A. Viergever, "Multiscale vessel enhancement filtering," in *Proc. Int. Conf. Med. Image Comput. Comput.-Assisted Intervention*, 1998, pp. 130–137.

[40] D. Stromer, V. Christlein, T. Schoen, W. Holub, and A. Maier, "Browsing through closed books: Fully automatic book page extraction from a 3-D X-ray CT volume," in *Proc. 14th IAPR Int. Conf. Document Anal. Recognit.*, 2017, vol. 1, pp. 224–229.

[41] S. Deitsch *et al.*, "Automatic classification of defective photovoltaic module cells in electroluminescence images," *CoRR*, vol. abs/1807.02894, 2018. [Online]. Available: http://arxiv.org/abs/1807.02894

Authors' photographs and biographies not available at the time of publication.